DRAFT VERSION JANUARY 25, 2016
Preprint typeset using LaTeX style emulateapj v. 01/23/15

arXiv:1601.05801v1 [astro-ph.HE] 21 Jan 2016

RESOLVING MICROLENSING EVENTS WITH TRIGGERED VLBI

MANSOUR KARAMI[1,2], AVERY E. BRODERICK[1,2], SOHRAB RAHVAR[4,1], MARK REID[3],
[1] Perimeter Institute for Theoretical Physics, 31 Caroline Street North, Waterloo, ON N2L 2Y5, Canada
[2] Department of Physics and Astronomy, University of Waterloo, 200 University Avenue West, Waterloo, ON N2L 3G1, Canada
[3] Harvard-Smithsonian Center for Astrophysics, 60 Garden Street, Cambridge, MA 02138, USA
[4] Sharif University of Technology, Azadi Ave. Tehran, Iran PO Box: 11365-11155
Draft version January 25, 2016

ABSTRACT

Microlensing events provide a unique capacity to study the stellar remnant population of the Galaxy. Optical microlensing suffers from a near complete degeneracy between the mass, the velocity and the distance. However, a subpopulation of lensed stars, Mira variable stars, are also radio bright, exhibiting strong SiO masers. These are sufficiently bright and compact to permit direct imaging using existing very long baseline interferometers such as the Very Long Baseline Array (VLBA). We show that these events are relatively common, occurring at a rate of ≈ 40 yr^{-1} of which 1.3 yr^{-1} are associated with Galactic black holes. Features in the associated images, e.g., the Einstein ring, are sufficiently well resolved to fully reconstruct the lens properties, enabling the measurement of mass, distance, and tangential velocity of the lensing object to a precision better than 15%. Future radio microlensing surveys conducted with upcoming radio telescopes combined with modest improvements in the VLBA could increase the rate of Galactic black hole events to roughly 10 yr^{-1}, sufficient to double the number of known stellar mass black holes in a couple years, and permitting the construction of distribution functions of stellar mass black hole properties.

Keywords: gravitational lensing: micro — masers — radio lines: stars — stars: black holes

1. INTRODUCTION

Gravitational lensing presents one of a handful of current observational windows on the dark universe. The distortion of background galaxies by galaxy clusters has provided a striking demonstration of general relativity (Bartelmann 2010). More importantly, it has enabled the unique reconstruction of the projected mass density of the cluster dark matter haloes (Refregier 2003; Paczynski 1986). While the dynamics of stars and gas probe the dark matter halo within 10^2 kpc of the central galaxy (Persic et al. 1996), gravitational lensing currently provides the only means to detect and study the halo on larger scales. By combining such measurements, it has become possible to map the dark matter distribution in the local universe (Shan et al. 2014).

The detailed structure of a gravitationally lensed image may be separated into the intrinsic structure of the lensed object and a distortion imposed by the lens that depends upon the lens location and mass distribution. A typical scale is set by the Einstein angle, this is exactly the angular scale of the Einstein ring cast by a point lens,

$$\theta_E = \sqrt{\frac{4GM(D_S - D_L)}{c^2 D_S D_L}}, \tag{1}$$

where M is the total source mass and D_S and D_L are the source and lens distance, respectively. For galaxy clusters this can span many arcminutes.

Gravitational lensing within the Galaxy also occurs when the angular separation of a background star and a foreground object becomes comparable to θ_E. This differs from the gravitational lensing of clusters and galaxies in two important respects. Firstly, the angular size of the lensed image has a typical scale of $\theta_E \approx 1(M/M_\odot)^{1/2}$ mas, well below the resolution of existing optical telescopes. As a result, direct optical imaging has not been feasible. Nevertheless, the conservation of brightness, a consequence of Liouville's theorem, implies substantial amplifications of the total flux associated with the magnified image, typically increasing by more than an order of magnitude. Secondly, the peculiar motions of objects within the Galaxy cause the source-lens system to evolve on timescales comparable to

$$t_E \equiv \frac{\theta_E}{|\boldsymbol{\mu}_S - \boldsymbol{\mu}_L|}, \tag{2}$$

where $\boldsymbol{\mu}_S$ and $\boldsymbol{\mu}_L$ are the source and lens apparent angular velocities, respectively. For typical values in the Galaxy t_E ranges from days to months, depending on the source mass and distance of lens and source from the observer. The relationship between t_E and the lens structure implies a characteristic light curve, referred to as a microlensing event.

The rarity of serendipitous lens-source alignments require the monitoring of large numbers of potential sources to identify candidate microlensing events. For this purpose optical surveys of dense star fields have been undertaken by a number of groups, both to constrain the contribution of stellar remnants to the Galactic dark matter budget (Moniez 2010) and more recently to find extrasolar planets which results in short timescale features in the microlensing light curve (Gaudi 2012). These have successfully excluded remnants with masses between $10^{-7}M_\odot$–$10M_\odot$ as a candidate for dark matter within the Galactic halo (Lasserre et al. 2000; Alcock et al. 2001).

Motivated by the potential to detect extra-solar planets, recent years have seen the initiation of high-cadence, large-area surveys. These have been enabled by the development of large CCD arrays for telescopes with wide fields of view. As a result, the OGLE[1] (Optical Gravitational Lensing Experiment) collaboration recorded $\approx 2 \times 10^3$ events in 2013, using the early warning system (Udalski et al. 1994) to alert the follow-up telescopes for monitoring microlensing events with higher precision. The Korean Microlensing Telescope Network (KMTNet) will increasing the number of events to 6000 per year with a 10 minute cadence operating continuously (Poteet et al. 2012).

[1] http://ogle.astrouw.edu.pl/ogle4/ews/ews.html

Reconstruction of microlensing events usually only determines the t_E. As a direct consequence, the mass of the lens, and the distances and velocities of the lens and source suffer from a fundamental degeneracy. Methods for breaking the mass-distance degeneracy typically requires higher-order effects. If the microlensing parallax can be measured – an asymmetry in the light curve induced by the non-uniform motion of the Earth – the lens distance and the mass of the lens can be constrained (Gould 1992; Rahvar et al. 2003). Parallax effect can also be employed by monitoring microlensing events from earth and space simultaneously. Spitzer has been used to this end, measuring microlensing parallax and thus providing an additional constrain (Street et al. 2015). Alternatively the source finite-size effect could be used to break the degeneracy. If the angular impact parameter is smaller than the source angular size the point source approximation is no longer valid and the finite-size effect becomes important. By analyzing the light curve an additional relation between angular source size and angular Einstein radius could be found. In both cases, the lens and the source apparent motions must be subsequently measured after the event to remove these from consideration (see, e.g., Gould 2014), which is only possible for stellar lenses and explicitly excludes those associated with stellar remnants.

Directly resolving the image would greatly simplify the reconstruction of the lens parameters. The typical scales of microlensing events are well matched to those achievable by very long baseline interferometry (VLBI) at centimetre wavelengths, e.g., with the Very Long Baseline Array (VLBA). Unfortunately, imaging microlenses with the VLBA requires compact radio bright sources with typical brightness temperatures in excess of 10^{10} K, well above the typical stellar temperatures. However, the unprecedented rate at which microlensing events are being identified by optical surveys makes it possible to leverage rare source properties for this purpose.

Mira variables provide a natural target for optically triggered radio imaging microlensing experiments.[2] Miras are asymptotic giant branch (AGB) stars with month time-scale pulsations largely determined by convection in their envelopes (Wood 2006). While the optical luminosities of Miras can vary over three orders of magnitude (Reid & Goldston 2002), the typical peak luminosities are on the order of $10^3 L_\odot$, ensuring that they are among the brightest objects in microlensing survey samples (Soszyński et al. 2013). Assuming there are 6×10^5 Mira stars in the bulge (Matsunaga et al. 2005), the optical depth of microlensing events should be $\tau \simeq 2.35\times10^{-6}$ in direction of Galactic bulge (Sumi et al. 2003) and a typical time scale of one month for the microlensing events (i.e. $< t_E > \simeq 1$ month), the rate of events with hundred percent detection efficiency can be obtained by

$$\frac{N_{events}}{N_{stars}T_{obs}} = \frac{2}{\pi}\frac{\tau}{< t_E >}. \quad (3)$$

We expect to observe roughly 11 Mira-source microlensing events per year. With typical masses similar to $1M_\odot$ Miras are relatively numerous despite having AGB lifetimes of roughly a million years.

Of particular importance here is the presence of SiO masers in the extended atmospheres of Miras. Typical sizes of the masing regions are 1 AU, corresponding to angular sizes of 0.1 mas for distances characteristic of bulge stars (Reid et al. 2007). Because of the nonthermal nature of the maser process, the spots can have brightness temperatures as high as 5×10^{10} K, well above the thresholds for imaging with the VLBA (Reid et al. 2007). Within the Galactic center, the inner parsec of the Galactic bulge, the SiO masers associated with evolved stars have been imaged with the VLBA at angular resolutions of 0.7 mas, limited by the interstellar electron scattering in that region (Reid et al. 2003, 2007). Outside of the Galactic center, it should be possible to image these with resolutions approaching 0.3 mas.

Here we explore the rates of suitable microlensing events anticipated by current and future surveys and the precision with which the associated lens parameters can be reconstructed. We propose using optical microlensing surveys to trigger follow-up VLBA observations based on source location in the color-magnitude diagram, anticipated event duration, and the lack of a bright lens counterpart. The color-magnitude diagram (CMD) provides a proxy for identifying Miras, if not already identified due to intrinsic variability. Massive lenses are more heavily represented in long-duration events, and those without obvious stellar counterparts are more likely to be associated with massive compact objects.

In section 2 we describe a Monte Carlo simulation of microlensing events, discuss the relative rates at which Miras are expected to be lensed by various objects, including stellar remnants, and how event selection can be optimized for imaging based on optical properties. Section 3 discusses the absolute rates of radio-bright black hole microlensing events of a variety of potential surveys. Section 4 describes the resulting images for a simple maser model and estimates the accuracy with which the lens properties can be reconstructed. The implications for constructing mass and distribution functions for the Galactic remnant population is discussed in 5. Finally, conclusions are collected in 6.

2. STELLAR REMNANTS IN SIMULATED MICROLENSING SURVEYS

The rates of microlensing events associated with compact remnants depends on the distribution of sources and lenses within the Galaxy and the detection efficiency of current and upcoming microlensing surveys. Here we describe simulations of an OGLE-like microlensing survey and estimate the number of microlensing events we anticipate to be associated with the various Galactic remnant populations. To do this, we perform mock surveys assuming the monitored stellar field is located in the Galactic bulge.

Necessary inputs are the mass, velocity, color, and magnitude distributions of potential sources and the mass and velocity distributions of potential lenses. For simulation of microlensing events, we adapt the detection efficiency in terms of the Einstein crossing time of OGLE survey sources (Wyrzykowski et al. 2015). We describe the details of the model here.

2.1. *Galactic Distribution Model and Stellar Lens/Source Population Model*

For generating microlensing events we need the spatial distribution of stars as well as their velocities.

For the structure of the Galaxy, we use thin disk model and standard bulge model from Binney & Tremaine (1987). The density distribution in disk is modeled in cylindrical coordi-

[2] Heyl (2011) explore a number of other potential radio-bright microlensing targets, including the continuum emission from a wide class of giants. Of these, only the SiO masers from Miras and active galactic nuclei have sufficiently high brightness temperatures to be amenable to VLBI imaging.

Table 1
Assumed parameters of the galactic model, The model is partly adopted from (Rahvar et al. 2003).

Structure	Parameter		Value
Disk	Σ ($M_\odot$ pc^{-2})		50
	H (kpc)		0.325
	R_d (kpc)		3.5
	velocity	σ_r km s^{-1}	34.
	disper-	σ_θ km s^{-1}	28.
	sions	σ_z km s^{-1}	20.
Bulge	M_B ($M_\odot$)		1.7×10^{10}
	a (kpc)		1.49
	b (kpc)		0.58
	c (kpc)		0.40
	velocity	σ km s^{-1}	110
Spheroid	ρ_0 ($M_\odot$pc^{-3})		0.932×10^{-5}
	a_c (kpc)		0.5
	velocity	σ km s^{-1}	120
Halo	$\rho_{H\odot}$ ($M_\odot$pc^{-3})		0.008
	R_c (kpc)		5.0
	M *in* 60 kpc ($10^{10}M_\odot$)		51
	velocity	σ km s^{-1}	200

nates by a double exponential functions,

$$\rho_D(R,z) = \frac{\Sigma}{2H}\exp\left(\frac{-(R-R_\odot)}{R_d}\right)\exp\left(\frac{-|z|}{H}\right), \qquad (4)$$

where Σ is the column density of the disk at the Sun position, H the height scale and R_d the length scale of the disk. The distribution of the lens transverse velocity with respect to the line of sight is established from the sun's proper motion within the thin disk and from the local velocity distributions (see Table 1).

The bar is described in a Cartesian frame positioned at the galactic center with the major axis x tilted by $\phi = 45^\circ$ with respect to the Galactic center-Sun line. The bar density is given by

$$\rho_B = \frac{M_B}{6.57\pi abc}e^{-r_s^2/2}$$
$$r_s^4 = \left[\left(\frac{x}{a}\right)^2+\left(\frac{y}{b}\right)^2\right]^2+\frac{z^4}{c^4}, \qquad (5)$$

where M_B is the bulge mass, and a, b and c are the scale length factors. The dispersion velocity of bulge stars is 110 km s^{-1}. For the density of the Spheroid structure we take the following function (Robin et al. 2003),

$$\rho_{spher} = \begin{cases}\rho_0(a_c/8.5\text{kpc})^{-2.44} & a \le a_c\\ \rho_0(a/8.5\text{kpc})^{-2.44} & a \ge a_c\end{cases} \qquad (6)$$

$a^2 = R^2+z^2/(0.76)^2$, a_c, ρ_c and spheroid velocity dispersion are given in table (1).

Combining the density distribution of Galaxy, kinematics, mass function and stellar population of stars, we can generate microlensing events in terms of t_E, M_l, D_l, D_s, θ_E and π, where π is the parallax parameter that is described in the Appendix. We use the detection efficiency of OGLE survey in terms of Einstein crossing time (i.e. $\epsilon(t_E)$) to select the observed microlensing events in our simulation (Wyrzykowski et al. 2015). A general overview about the simulation of microlensing events can be found in Rahvar (2015).

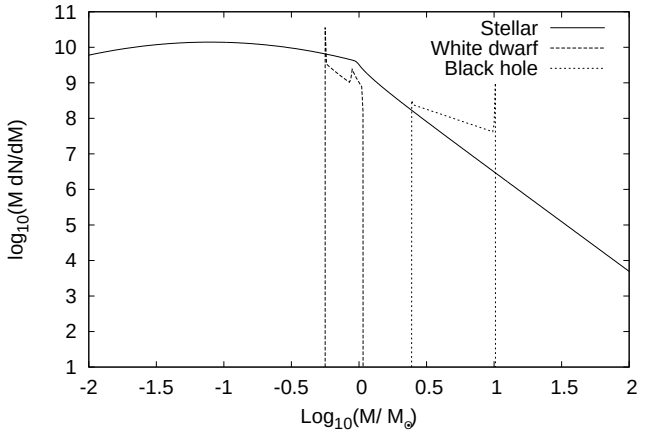

Figure 1. Assumed mass functions of stars (solid), white dwarfs (dashed), and black holes (dotted) in the disk and bulge. The spike features at low (white dwarf) and high (black hole) masses correspond to regions in which the remnant mass is nearly independent of that of the progenitor. These do not substantially impact the results here.

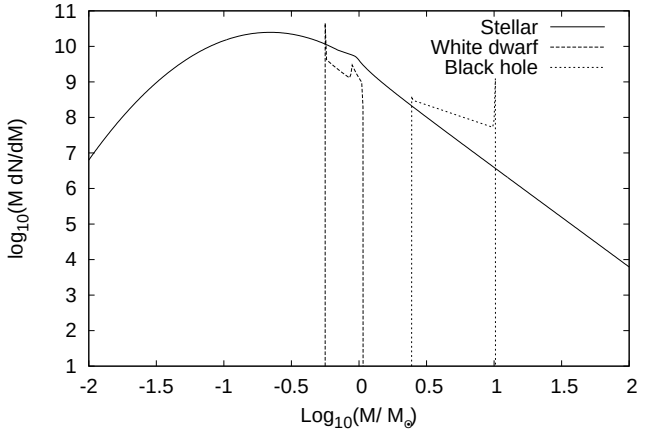

Figure 2. Assumed mass function of stars (solid), white dwarfs (dashed), and black holes (dotted) in the Spheroid. The spike features at low (white dwarf) and high (black hole) masses correspond to regions in which the remnant mass is nearly independent of that of the progenitor. These do not substantially impact the results here.

2.2. Remnant Population Model

In addition to the known stellar populations, gravitational lens candidates include the Galactic population of compact objects. In principle, these may be comprised of the remnants of stellar evolution and primordial objects. We make the conservative assumption that the latter are absent, and consider only the remnants of massive stars.

The end point of stellar evolution depends primarily on the mass of the progenitor. We consider two classes of remnants, white dwarfs and black holes. We ignore the intermediate neutron stars, which we expect to contribute marginally to the high-mass tail of the white dwarf population and otherwise be indistinguishable from them using microlensing observations alone. Hence in practice the remnants are effectively white dwarfs/neutron stars and black holes.

Encoded in the remnant population is the Galactic high-mass star formation history. Once the relationship between the zero-age main sequence progenitor mass ($M_{\rm MS}$) and the final remnant mass (M_R, where R may be WD or BH) is specificed, the

mass function[3] ($\phi(M_R)$) is given solely in terms of the star formation rate ($\Lambda(t)$) and initial mass function of main sequence stars ($\Phi(M_{\rm MS})$):

$$\phi(M_R) = \int dt \frac{\Lambda(t - T_{\rm MS})\Phi(M_{\rm MS})}{d\log_{10} M_R / d\log_{10} M_{\rm MS}}, \quad (7)$$

where $T_{\rm MS} \approx 10(M_{\rm MS}/M_\odot)^{-1.5}$ Gyr is the lifetime of a main sequence star with mass $M_{\rm MS}$ associated with the remnant mass M_R, and the integration is over the entire Galactic history. Effectively, this is simply the number of remnants formed over the history of Galactic star formation, excluding those stars that remain on the main sequence. For this we adopt the star formation rate from Hartwick (2004), which peaks roughly 10 Gyr ago, and the "Disk and Young Clusters" stellar initial mass function (IMF(M)) from Chabrier (2003), though employing the "Universal" IMF from Kroupa (2001) makes no discernible difference.

We relate $M_{\rm WD}$ and $M_{\rm MS}$ via the piecewise continuous expression presented in (Salaris et al. 2009), obtained for white dwarfs in open clusters by comparing the white dwarf ages inferred by cooling models and cluster age from isochrone fitting:

$$M_{\rm WD}/M_\odot = \begin{cases} 0 & m_{\rm MS} \leq 0.5588 \\ 0.01 m_{\rm MS} + 0.5418 & 0.5588 < m_{\rm MS} \leq 1.7 \\ 0.134 m_{\rm MS} + 0.331 & 1.7 < m_{\rm MS} \leq 4 \\ 0.047 m_{\rm MS} + 0.679 & 4 \leq m_{\rm MS} < 8 \\ 0 & 8 \leq m_{\rm MS}, \end{cases} \quad (8)$$

where $m_{\rm MS} \equiv M_{\rm MS}/M_\odot$.

The relationship between $M_{\rm BH}$ and $M_{\rm MS}$ is highly dependent upon the uncertain evolution of massive stars and the details of core collapse supernovae. As a result, above $30M_\odot$ it is unclear what the slope of the $M_{\rm BH}$-$M_{\rm MS}$ relationship is (see Figure 9 of Fryer et al. 2012). Here we make a moderately conservative assumption that the resulting black hole mass is independent of $M_{\rm MS}$, setting

$$M_{\rm BH}/M_\odot = \begin{cases} 0 & m_{\rm MS} \leq 8 \\ 0.3 m_{\rm MS} & 8 < m_{\rm MS} \leq 33 \\ 10 & 33 < m_{\rm MS}, \end{cases} \quad (9)$$

which lies in the middle of the permitted range presented in Fryer et al. (2012) and is roughly consistent with narrow black hole mass range inferred from X-ray binaries by (Özel et al. 2010).

The resulting stellar and remnant mass functions for the disk, bulge and spheroid are shown in Figures 1, 2. The spikes in the low and high mass ends of the white dwarf and black hole mass functions are associated with regions in which the remnant mass are nearly independent of the progenitor mass, and contain a finite number of objects. For both the disk and the bulge there is a break in the stellar mass function where stars produced during the star formation peak are leaving the main sequence, roughly $1M_\odot$.

Because neither white dwarfs nor black holes are expected to experience strong kicks at formation, we assume the same velocity dispersion for the remnants as the surrounding stellar population. This is notably not the case for neutron stars, which often experience sufficient kicks to be launched into the halo, diluting their density in the disk and therefore their representation in the lens sample for current and planed microlensing surveys.The observation of pulsars with ages less than 3 Gyr, indicates the pulsar birth velocity of about 400 km s^{-1} (Hobbs et al. 2005).

[3] We define the mass function to be the number of objects per logarithmic decade, i.e., $dN/d\log_{10} M$.

2.3. Mock Observation Statistics

In order to simulate the microlensing events, we choose the source stars from a Hipparcos like color-magnitude distribution, distributed proportional to the density of matter. After selecting the source star with a given absolute color and magnitude, the position of star in the color–magnitude diagram changes due to the distance modulus and interstellar extinction. Those stars brighter than the limiting magnitude of the microlensing survey (which is taken about 19 in this simulation) are selected for the observation. It should be noted that the results are not sensitive to the limiting magnitude and could be applied to microlensing surveys with different limiting magnitudes.

We note that all the microlensing events generated in this simulation are not observable in reality. Depending on duration of observation, cadence of photometric data and non-observing nights due to bad weather and technical failures, only a fraction of events as a function of Einstein crossing time, t_E, can be observed. We adapt the detection efficiency function (i.e. $\epsilon(t_E)$) for selecting the observed events from OGLE published function (Wyrzykowski et al. 2015). Detailed description about gravitational microlensing formalism can be found in Rahvar (2015).

Each event is constructed by first choosing a random source with the appropriate properties, subsequently a random lens with the appropriate properties, and finally applying the OGLE detection efficiency. That is,

1. Source star selection:
   (a) A source star position is selected with a probability distribution given by the stellar density and geometric factors, i.e.,
   $$\frac{dP}{dD_S} \propto \rho(D_S) D_S^2, \quad (10)$$
   (b) The source star stellar type is randomly chosen according to Hipparcos Color-Magnitude distribution.
   (c) The stellar component (bulge, disk, spheroid) is selected with weights equal to their density at D_S.
   (d) The source star velocity is the sum of the bulk Galactic motion for the chosen stellar component at the chosen source location and a random contribution pulled from a Gaussian distribution with the appropriate dispersion (listed in Table 1).
2. Lens selection:
   (a) A lens position is selected from the stellar density, modified by the lensing cross section, i.e.,
   $$\frac{dP}{dD_L} \propto \rho(D_L) \sqrt{\frac{D_L(D_S - D_L)}{D_S^2}}. \quad (11)$$
   (b) A lens component (bulge, disk, spheroid) is randomly chosen according to the local densities of each at D_L.
   (c) A lens component type (star, white dwarf, black hole) is randomly chosen according to the local fraction of each for the given component.

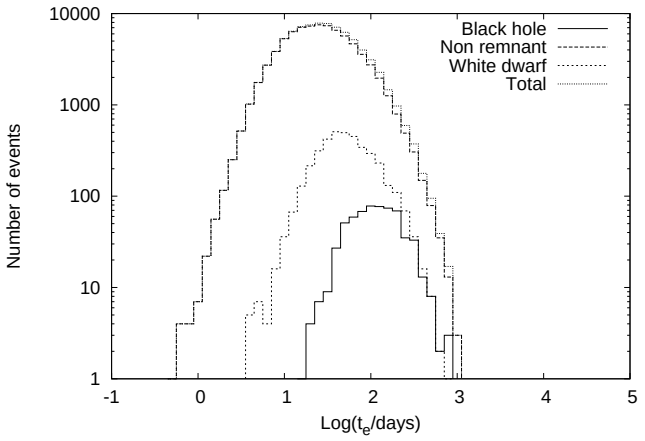

Figure 3. Distribution of microlensing events in Einstein crossing time from Monte-Carlo simulation. The detection efficiency of OGLE IV survey is applied during event selection. The fraction of black hole events to the overall events is 0.035 and weighted heavily towards long t_E.

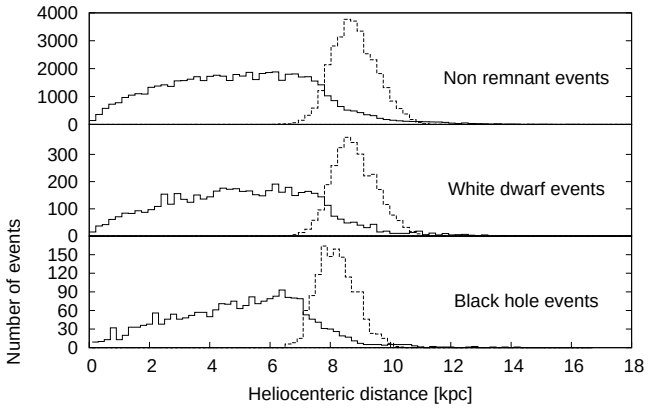

Figure 4. Distribution of lens positions in galaxy for various lens populations. Contributions of the disk (solid) and bulge (dashed) are shown separately; the spheroid contribution is negligible.

(d) A lens mass is selected according to the total mass function of the chosen component modified by the approximate lensing cross section; for a fixed observing time the probability of detecting a lens is $\propto \theta_E \propto M^{1/2}$.

(e) A lens velocity is the sum of the bulk Galactic motion for the chosen component and a random contribution pulled from a Gaussian distribution with the appropriate dispersion (listed in Table 1).

3. Detection efficiency cut: Given the lens mass, source and lens velocities, and source and lens positions t_E is computed, and the event is accepted with a probability set by the OGLE detection efficiency.

The result is a set of lensing events with known intrinsic properties (source and lens masses, distances, velocities, and types) selected using a realistic microlensing survey biases.

Figure 3 shows the distribution in Einstein crossing time of simulated events. Since in the simulation we flag lenses that are either main sequence or remnants and, we can classify lenses based on lens type. Here we compare the overall microlensing events with those produced by black holes specifically; the fraction of events with black hole lenses is 0.035. This fraction is comparable to the estimate of Gould (2000), which finds 0.01 assuming a 100% detection efficiency, and thus neglecting the higher detection efficiency of Mira events.

Another important point is the average t_E for the overall events and black hole events are 38 days and 127 days, respectively. This is unsurprising since the duration of events scales with lens mass as $M^{1/2}$, and is an immediate consequence of the fact that the average black hole mass is roughly an order of magnitude larger than that of the overall sample. Hence, black hole lensing events are typically more than three times longer than the typical microlensing event, with important consequences for identification and parameter estimation.

Figure 4 shows the distribution of lens locations in our simulated survey for each of the Galactic components and lens types. Events are dominated by lenses within the disk (65%) with the remainder from the bulge (35%); the spheroid contributes negligibly. Of note is that the lens distribution within the disk is nearly evenly distributed between the bulge and a heliocentric distance of 2 kpc, implying that microlensing surveys necessarily probe the lens population throughout the intervening disk. This remains true independent of the lens type.

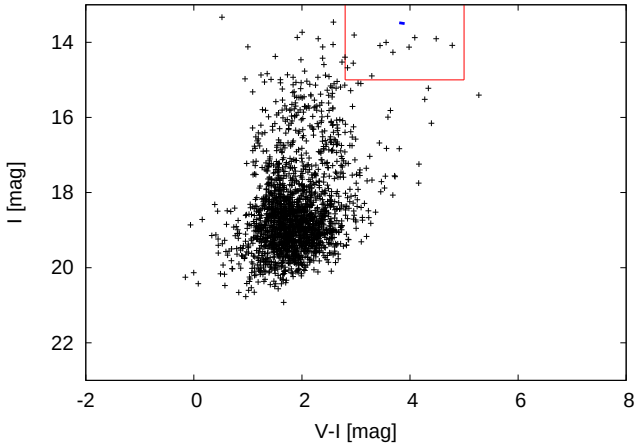

Figure 5. Color-Magnitude diagram for OGLE III Microlensing events. Half of the stars in the red box are likely to be Mira variables. The small blue line inside the red box shows how much a MIII giant will move in HR diagram as a result of blending with a solar type (G2V) lens star located half way between the source and observer.

3. RADIO-BRIGHT MICROLENSING EVENT RATES

Key to the radio imaging of microlensing events is the identification of radio-bright lensed sources. In the near term this requires the identification of candidate events based on their optical properties alone. Here we discuss the rates implied by the previous section employing surveys that exploit optical counterparts of radio bright sources (i.e., Mira variables) and the potential rates from future radio microlensing surveys. This is ultimately dependent on the population and distribution of candidate sources.

3.1. Miras as Microlensing Sources

Miras provide a natural class of optically bright sources with strong radio emission in the form of circumstellar SiO masers. In most microlensing surveys Miras have already been identified due to their variable nature. Where they have not, they are readily identified in the optical color magnitude diagram. (Figure 5). Importantly, there is little chance for source confu-

sion – blending of source and lens stars does not move objects appreciably within the region populated by Miras.

The variable nature of Miras provide an immediate impediment to their use as microlensing survey targets; typical Miras vary with periods of ≈ 1 yr, I-band variability amplitudes between 1.4 mag and 3 mag (Soszyński et al. 2013), and V-band variability amplitudes typically two–three times larger (Kholopov 1990). However, black hole microlensing events can be easily distinguished from the intrinsic variability as a result of three important differences. All of these may be exploited in part due to the high luminosity of Miras, and therefore the high photometric accuracy with which they may be monitored.

Firstly, microlensing light curves have a well-understood and uniform structure set by the lens-source geometry and nature of gravitational lensing, characterized by a divergent rise as the source approaches the lens caustics (moderated by the finite source size). This differs starkly from the smooth intrinsic variations of Miras. Thus careful light curve fitting should be able to rapidly distinguish between microlensing and intrinsic variability.

Second, the amplitude of the flux variation during microlensing events is typically larger than that due to intrinsic variability. Typical magnifications are of order 450%, while high-magnification events can exceed an 1000%. These correspond to magnitude variations of 1.5 mag and 2.5 mag, comparable the that caused by intrinsic variations in I-band. Hence, the microlensing signal is an order unity modification of the underlying source variability in I-band. At longer wavelengths the intrinsic variability decreases further, on average variations in the magnitude at 1.25 μm are 20% of those at optical wavelengths (Smith et al. 2002)[4].

Thirdly, the flux variations due to microlensing are achromatic. Again this is in stark contrast to the intrinsic variability of Miras, which varies dramatically with wavelength. Thus, multi-band monitoring should be readily able to disentangle the two variability components.

3.2. *Bulge Miras Microlensing Rates*

The OGLE III survey monitored approximately 150 million stars in Galactic bulge from 2001 to 2009 in search for gravitational microlensing events and provided us with the largest catalogue of microlensing events available. OGLE used the Early Warning System (EWS) to detect ongoing microlensing events (Udalski et al. 1994). EWS uses Difference Image Analysis photometry and by analyzing all the stars in the field flags the potential microlensing events (Alard & Lupton 1998). In doing so it currently identifies and filters out variable stars. The flagged stars go through several tests including a visual inspection of the light curve and after satisfying all the criteria they are announced as a microlensing candidate.

We used OGLE III microlensing alerts data (2002 - 2009) to find the relative number of Mira-type candidates, demonstrating their high detection efficiency (though note that all Miras will have been excluded). Of all the 4052 events 2015 had both V and I magnitudes available which were used for our analysis. The events which only have I band measurements would not have a substantial contribution to M III stars, since they are mainly faint stars. Figure 5 shows the CMD for these events together with the box to select type M III stars. These are a few orders of magnitude brighter than M-dwarfs, increasing their representation in microlensing surveys. An advantage of using bright stars is that blending by background and lens stars do not affect the brightness of the source star significantly (Figure 5). Moreover, from the lens equation, and estimating the mass of the lens star, we can calculate the contribution of blending and correct the position of source star in CMD (Muraki et al. 2011; Miyake et al. 2011).

Within the OGLEIII catalogue there are currently 6528 Miras (Soszyński et al. 2013). The larger number of Miras inferred in the bulge suggest that this can be readily enlarged by surveying the entire bulge region. Estimates based on the OGLEII catalogue suggest as many as $\approx 6 \times 10^5$ Miras in Galactic Bulge (Matsunaga et al. 2005). The large luminosities of Miras implies a near unity detection efficiency, and thus as discussed around equation (3), we anticipate a total bulge-Mira microlensing event rate of 11 yr^{-1}. Therefore, monitoring the Galactic Bulge alone will produce ≈ 0.4 black hole microlensing events per year associated with a radio-bright source, enabling radio imaging.

3.3. *Current and Near-future Optical Survey Microlensing Rates*

At least two future microlensing surveys are underway, exceeding OGLE III in three ways: higher cadence, deeper magnitude limits, and increased sky coverage. OGLE IV, in operation since 2010, has a bulge field of ≈ 330 deg^2, 3.3 times larger than that of OGLE III. The resulting OGLE IV EWS event rate is three times larger than that of OGLE III; OGLE III EWS detected about 650 events in 2008 whereas OGLE IV EWS detected almost 2000 events in 2013 and over 2000 in 2014. The forthcoming The Korean Microlensing Telescope Network (KMTNet) consists of three dedicated 1.6 m telescopes located in Australia, South Africa, and South America, each with 4 deg^2 field of view. Thus, KMTNet anticipates detecting ≈ 2300 microlensing events per year with constant cadence of almost 10 min (Henderson et al. 2014).

The high luminosity of Miras and the long time-scales of black hole microlensing events imply that the first two, higher cadence and deeper magnitude limits, will at best produce modest improvements in the Mira microlensing rate. High cadences will vastly over-sample black hole microlensing light curves, and thus while important for planet searches are unlikely to be helpful for the study of Galactic remnants.

Even within the extincted region near the Galactic center Miras remain visible due to their high intrinsic luminosity. Since optically dim stars do not produce strong radio emission (Stellar photospheres of dwarf stars are essentially undetectable with current radio telescopes), expanding the survey sample to less luminous objects provides little value for the study of black holes. Nevertheless, the deeper magnitude limits of future surveys will permit the inclusion of regions of high extinction, i.e., dark areas of the bulge, in survey fields (Schultheis et al. 2009), marginally increasing the number Miras that can be monitored. This may be ameliorated by operating microlensing surveys in the infrared as well.

Much more important is the expanded sky coverage. We have already assumed that the entire Galactic bulge will be monitored in our previous rate estimate. Further increasing the number of monitored Miras substantially in an optical survey necessarily requires expanding the surveys beyond the bulge. Moderate modifications to the observing strategies of existing optical surveys present an obvious way in which radio-bright

[4] There are instances for which near-infrared variability is nevertheless sizable, e.g., R Cas, where the amplitude of variations at 1.25 μm are as large as 1.42 mag. However, the variability continues to drop rapidly with increasing wavelength.

microlensing event rates can be substantially increased. Because Miras are intrinsically luminous, they lie well above the detection threshold of all ongoing microlensing surveys located anywhere within the Galaxy. Therefore, the relative paucity of Miras does suggest an alternative strategy: broad and shallow instead of narrow and deep.

Including the Galactic disk is expected to grow the Mira sample by a factor of $\approx$ 6-7 assuming the stellar population does not vary widely between the bulge and the disk. Hence, we expect $\approx 4\times10^6$ Miras in total within Milky way. Unfortunately, the microlensing optical depth in the disk is roughly a third of that of the bulge as a result of the former's smaller stellar density. Taking into account the smaller optical depth in the disk a survey that monitors the entire Galactic plane to a magnitude limit of 15 would capture radio-bright microlensing events at a rate of 37 yr^{-1}, corresponding to a radio-bright black hole microlensing events at a rate of 1.3 yr^{-1}. This is sufficient to double the number of known Galactic black holes within less than two decades.

Importantly, these survey strategies need not be exclusive. Since the objects of primary interest for radio imaging, black holes, result in long-duration microlensing events, even sparse time sampling is sufficient (on the order of once per week). The OGLE IV survey has already adopted such a strategy, monitoring the entire Galactic disk with a cadence of 1-2 days and the bulge with a cadence $\lesssim$ 1 hr (Udalski et al. 2015).

3.4. *Far-future Optical Microlensing Surveys*

The LSST (Large Synoptic Survey Telescope) is a 8.4 meter telescope equipped with a wide field camera with 9.6 square degrees field of view. It will provide a deep survey of southern sky (over 20000 square degrees) giving 1000 exposures of each patch during 10 years of observations. The optimal cadence of the survey for different areas of the sky is yet to be determined. The single exposure depth in r-filter will be $\approx$ 24.5 mag and it can yet go deeper ($\approx$ 26.5 mag) by co-adding the images. Being a ground base survey the angular resolution is limited by seeing (0".7) and ultimately by its pixel size (0".2) (Ivezic et al. 2008).

The mean cadence of $3-4$ days is much shorter than the typical time-scales of the long duration black hole lensing events. Furthermore the deep survey combined with the fact that Mira variables are bright stars guarantees that most of the Mira lensing events in the Galaxy, LMC, and SMC will be detected by LSST. Thus, for finding black hole lensing events amenable to radio imaging, the LSST presents a similar capability to current generation microlensing surveys operated with modified observation strategy.

3.5. *A Future Radio-Continuum Microlensing Survey*

Were a microlensing survey performed in the radio directly the need to identify optically-bright radio counterparts would be eliminated altogether, resulting in the finding of events that are amenable to radio imaging with a near 100% efficiency. Moreover such a radio survey would permit monitoring the much more numerous compact continuum radio sources. With the advent of a number of rapid-survey radio telescopes (e.g., the Square Kilometre Array Taylor 2007, Canadian Hydrogen Intensity Mapping Experiment Bandura et al. 2014, etc.), enabling rapid nearly all-sky surveys, high-cadence radio transient searches will become common. A radio microlensing survey is a natural byproduct of these.

The stringent requirements on source size ($\lesssim$ 1 mas) restricts the potential radio microlensing survey source targets to stars (e.g., Miras) or primarily extragalactic objects. The details of the lens parameter estimation are only weakly dependent on the distance to the radio source; placing sources at extragalactic distances decreases the Einstein angle by at most 30%.

More important is the over-all number of sources, which directly translates into the predicted rate enhancement. These, in turn, depend on the flux limit and wavelength of interest, both set by the VLBA. For a $10\,M_\odot$ black hole lens multiple image components are easily visible by the VLBA for frequencies above 3 GHz, providing a natural upper limit of 10 cm on the observation wavelength. For 10 min integration times with 500 MHz bandwidths the VLBA flux limit should be near 20 μJy and 40 μJy at 22 GHz and 43 GHz, respectively; where required we adopt a flux limits of 30 μJy.[5] Large-amplification events will reduce the effective flux limit further. As we will see below, either improvements in the sensitivity of the VLBA or new radio-bright source classes will be necessary to leverage a radio microlensing survey.

Radio-bright active galactic nuclei (AGN) provide a natural class of sources, being both numerous, and more importantly compact. Conveniently, they are also typically flat-spectrum radio sources, meaning that neither the source identification nor the subsequent microlensing survey need be performed at the same wavelengths at which the events are ultimately imaged. Thus, to estimate the number of potential sources above the VLBA flux limit we employ the NRAO VLA Sky Survey at 1.4 GHz reported in Condon et al. (1998) (though see also Condon 1984; Condon et al. 2012) finding roughly 1.6×10^7 and 1.5×10^8 radio-bright AGN in ellipticals and spirals, respectively, with fluxes above above 30 μJy.

These are distributed isotropically, and thus a large fraction of AGN will be visible at high Galactic latitude with correspondingly smaller lensing optical depth. As a result, the average lensing optical depth for an AGN survey to that for the optical surveys that monitor the Galactic bulge alone is approximately 0.01. Thus, despite having nearly 290 times the number of targets, a radio microlensing survey of objects above 30 μJy would produce a black hole microlensing event rate 1 yr^{-1}, about the same as that from Mira-based optical surveys.

To obtain an event rate of 10 yr^{-1}, doubling the number of know black holes in two years, requires a flux limit of 3 μJy. This is would require corresponding improvements in the VLBA. However, in principle this may be achieved via an extended integration time combined with an expanded bandwidth. Currently, 4 GHz bandwidths supported by 16 Gbps recorders are planned stations participating in millimetre-wavelength VLBI observations (Whitney et al. 2012), and could be deployed to VLBA stations for use at centimetre wavelengths. Combined with 2 hr integration times, these reach the 3 μJy flux limit needed. Below 3 μJy the number of sources scale approximately as $N_{>S}\propto S^{-0.5}$, and thus further growth in the number of sources is a slow function of flux limit.

4. RADIO VLBI EVENT RECONSTRUCTION

Motivated by the prospect of substantial number of optical microlensing events amenable to radio imaging, we now present illustrative examples of what these may look like for typical event parameters, and discuss the precision with which

[5] We assume system-equivalent flux densities are roughly 500 Jy and 1000 Jy at 22 GHz and 43 GHz, respectively.

the event parameters may be reconstructed.

4.1. Models of Resolved Masers

SiO masers at ≈ 43 GHz (≈ 7 mm) have routinely been detected around late-type giants in the central parsec of the Galaxy (Reid et al. 2003). Located within the extended atmospheres of Miras, these are typically within 8 AU of their parent, corresponding to an astrometric offset of 1 mas in the Galactic center. Note that this is comparable to the Einstein angle, θ_E, and therefore the lensing of the maser emission is distinct from that of optical emission of the star due to the finite size effect of source star (Witt & Mao 1994).

The masing spots are resolved both because of their intrinsic structure and as a result of an interstellar scattering screen that scatter-broadens images of the Galactic center (Backer 1978; Bower et al. 2006; Gwinn et al. 2014). Because of the latter effect, even point sources exhibit an extended source structure with a full-width half-max (FWHM) of ≈ 0.7 mas, effectively limiting longest baselines that can be employed by the VLBA. However, this scattering is highly localized, occurring only for sources in the immediate vicinity of the Galactic center, and unlikely to limit the resolution attainable by efforts to image Miras throughout the Galactic bulge.

Typical intrinsic sizes for nearby SiO individual maser spots are 1 AU, corresponding to ≈ 0.1 mas at ≈ 8 kpc distance, and therefore also unlikely to significantly limit the resolution of VLBA observations. We ignore the impact of intervening scatter broadening and model the intrinsic emission from an individual spot by a Gaussian intensity profile with a FWHM of 0.1 mas:

$$I_{\rm int}(\boldsymbol{\beta}) = I_0 e^{-|\boldsymbol{\beta}|^2/2\sigma^2_{\rm spot}}\,, \tag{12}$$

where $\sigma_{\rm spot} = 0.1\ {\rm mas}/\sqrt{8\ln 2} = 0.042$ mas.

In practice, SiO masers from Mira variables often form arc-like structures that are dominated by a handful of individual masing spots. For black hole lenses the angular sizes of these structures are typically smaller than θ_E, and thus multiple spots are likely to be strongly lensed simultaneously. For less massive lenses the ring angular angular scale and θ_E may be more similar. Nevertheless, because the emission between maser spots remains incoherent[6]. the resulting lensed image is a linear superposition of a number of individual spots. Thus, here we consider the simpler problem of a single masing spot to assess the size of the constraints that can be placed on the lens in principle.

Net velocity offsets between the star and masing spots are systematically incorporated into the radio source velocities and thus do not present an additional systematic uncertainty. However, the masing spots can also evolve in size and luminosity. Both are unlikely to produce substantial complications since it doesn't impact the separation of the lense images (see Section 4.4). While the latter can complicate the determination of the radio light curve, this may be ameliorated via the optical light curve.

4.2. Generating Mock Images

Time sequences of mock images are generated via a multi-step process: beginning with the specification of the positions of the source, lens, and observer, the mapping of the source to the image plane via the thin-lens equation, and convolution with a realistic beam.

[6] This is distinct from, e.g., for pulsars, which produce many *coherent* spots due to scintillation within the interstellar medium, and therefore require careful consideration of wave-optics effects (Pen et al. 2014).

Over the duration of a lensing event, the position of the source and lens are assumed to evolve with a fixed velocity:

$$x_S = x_{s,0} + v_S t \quad \text{and} \quad x_L = x_{L,0} + v_L t\,, \tag{13}$$

respectively. In practice only the transverse motion is important. In contrast, the observer position, i.e., that of the Earth, is orbital, and thus includes the orbital acceleration:

$$x_\oplus = x_{\oplus,0} + \int dt\, \boldsymbol{\Omega}_\oplus \times r_\oplus\,. \tag{14}$$

The lens geometry is then fully defined by the distances

$$D_L \equiv |x_L - x_\oplus| \quad \text{and} \quad D_S \equiv |x_S - x_\oplus|\,, \tag{15}$$

and the transverse angular displacement

$$\boldsymbol{\beta} \equiv \frac{(x_S - x_\oplus)}{D_S} - \frac{(x_S - x_\oplus)}{D_S}\cdot\frac{(x_L - x_\oplus)}{D_L}\frac{(x_L - x_\oplus)}{D_L}\,. \tag{16}$$

Neglecting the acceleration in the Earth's motion and the line-of-sight motion of the source and lens permits a simplification of $\boldsymbol{\beta}$ to a linear function of time, though here we will make use of the more general expression in equation (16).

For a point-mass lens the observed position on the sky, $\boldsymbol{\theta}$ is given by the thin-lens equation. Usually this is expressed as a potentially multi-valued function of the projected source position. However, we need only to identify the projected source position in terms of the observed position $\boldsymbol{\theta}$, given by

$$\boldsymbol{\beta} = \boldsymbol{\theta}\left(1 - \frac{\theta_E^2}{|\boldsymbol{\theta}|^2}\right)\,. \tag{17}$$

Since surface brightness is conserved, this then immediately defines the lensed image in terms of the intrinsic

$$I_{\rm lens}(\boldsymbol{\theta}) = I_{\rm int}\left[\boldsymbol{\beta}(\boldsymbol{\theta})\right]\,. \tag{18}$$

Finally, we convolve the lensed image with a realistic, if not pessimistic, beam. For this we assume a 43 GHz beam, $B(\boldsymbol{\theta})$ is an anisotropic Gaussian, consistent with the beam in Lu et al. (2011): semi-minor axis of 0.5 mas and semi-major axis of 1.4 mas, oriented 12° East of North. The large aspect ratio is a result of a combination of the low declination of the Galactic center and the North American location of the VLBA antennae. In practice, this resolution is lower than may be achieved by the VLBA at 43 GHz; in Reid et al. (2003) the interstellar scatter broadening limited the size of the array that could be effectively employed. Outside of the Galactic center it should be possible to increase the resolution by a factor of 2–3, though we adopt the Lu et al. (2011) beam. The resulting observed intensity distribution is then

$$I_{\rm obs}(\boldsymbol{\theta}) = \int d^2\theta' B(\boldsymbol{\theta} - \boldsymbol{\theta}') I_{\rm lens}(\boldsymbol{\theta}')\,, \tag{19}$$

where prior to the convolution the angular positions are converted into equatorial coordinates.

All that remains is to specify the relative positions, velocities, and mass of the source and lens. We do this for a handful of illustrative examples in the following sections.

4.3. Example Lensed Maser Images

As fiducial source parameters we assume $D_S = 8$ kpc and a proper velocity of 120 km s^{-1}, consistent with sources in Galactic bulge. The fiducial lens parameters are $D_L = 4$ kpc and a proper velocity of 30 km s^{-1}, consistent with the velocity dispersion in the Galactic disk. The relative positions of the source and lens are chosen so that minimum impact parameter is 0.3 mas oriented in declination. These result in typical

images that are illustrative of the general situation. All that remains is to specify the mass of the lens.

The first case we consider is that of a $10M_\odot$ black hole, for which $\theta_E = 3.2$ mas. A time-sequence of images for our fiducial case is shown in Figure 6, covering nearly a year. Since the minimum impact parameter is small in comparison to θ_E, multiple images are present. Because θ_E is also considerably larger than the intrinsic source and beam sizes, these are well resolved, suggesting that detecting and interpreting the features of strong lensing by black holes will be straightforward. In particular, a direct measurement of θ_E is possible simply by fitting the spot separations, though we defer to how well this may be done in practice to Section 4.4.

The same qualitative conclusions hold for a $1M_\odot$ lens, indicative of a white dwarf, shown in Figure 7.[7] Despite the smaller Einstein angle ($\theta_E = 1.0$ mas), multiple images are resolved, again implying that θ_E can be directly measured. Where these differ most dramatically is near peak magnification (center panel in Figures 6 and 7); the more massive lens produces correspondingly larger distortions in the image as a result of the better resolution of the Einstein ring. The microlensing event is also significantly shorter.

The effect of the accelerated observer frame, due to the Earth's orbital motion, is evident in the asymmetric entrance and exist from the microlensing event. However, this effect may be confused with features arising from the impact of the asymmetric beam and arbitrary event orientation. Thus in Figures 6 and 7 we have also shown by the red contours the images with the Earth's orbital motion neglected. From these it is clear that asymmetry in the temporal evolution of the image structure at early and late times is a robust indicator of parallax.

4.4. Parameter Estimation

The primary parameters of interest are those of the lens: mass, velocity, distance. Given only the magnification light curve these are degenerate, constrained only by the event timescale and peak magnification.[8] As a consequence, all that can be recovered even in principle are the projected impact parameter in unites of θ_E, t_E, and the time of maximum magnification. However, images like those in Figures 6 and 7 introduce at least two key additional observables: θ_E and a lensing parallax.

The peak magnification occurs at the projected closest approach, for which the projected impact parameter is $\beta_{\rm min}$ and the magnification is

$$A_{\rm max} = \frac{\beta_{\rm min}^2 + 2\theta_E^2}{\beta_{\rm min}\sqrt{\beta_{\rm min}^2 + 4\theta_E^2}}. \tag{20}$$

The degree to which $A_{\rm max}$ may be measured depends upon the quality of the photometry that can be performed, and thus is likely to be limited by systematic errors in the radio flux calibration (flux calibration accuracy for the VLBA and the VLA at 43 GHz would be roughly 10%). At this time the separation between the centroid of the primary and secondary images is

$$\Delta\theta = \sqrt{\beta_{\rm min}^2 + 4\theta_E^2}, \tag{21}$$

which may be measured directly from the images to a precision that exceeds the interferometric beam width by up to an order of magnitude for high signal-to-noise detections (Reid et al. 2003). Thus, together, these yield a high-precision estimate of θ_E:

$$\begin{aligned}\theta_E &= \frac{\Delta\theta}{\sqrt{2}}\left[A_{\rm max}\sqrt{A_{\rm max}^2 - 1} - (A_{\rm max}^2 - 1)\right]^{1/2} \\ &\approx \frac{\Delta\theta}{2}\left(1 - \frac{1}{8A_{\rm max}^2}\right),\end{aligned} \tag{22}$$

where the latter expression is for large $A_{\rm max}$, and a fractional precision of

$$\frac{\sigma_{\theta_E}^2}{\theta_E^2} \approx \frac{\sigma_{\Delta\theta}^2}{\Delta\theta^2} + \frac{\sigma_{A_{\rm max}}^2}{4A_{\rm max}^6}. \tag{23}$$

When the uncertainty is dominated by the astrometric uncertainty, this implies that for a $10M_\odot$ black hole θ_E can be measured to within $\approx 1\%$.

Even without detailed event modeling, θ_E immediately enables the determination of the relative angular lens-source velocity from equation (2):

$$\boldsymbol{\omega}_L - \boldsymbol{\omega}_S = \frac{\theta_E}{t_E}\hat{u}, \tag{24}$$

where $\hat{u}$ is the asymptotic direction of the vector between the first and second images. The source proper motions can be directly measured by follow-up observations; the angular velocities of individual maser spots have been measured with an accuracy better than 1 mas yr^{-1}. As with the source positions, this is limited by the electron scattering Reid et al. (2003), and thus for sources beyond the central pc it should be possible to measure this nearly an order of magnitude better, giving a typical accuracy of 0.1 mas yr^{-1}, corresponding to a physical velocity of 4 km s^{-1} at the distance of the Galactic center. With a typical lens apparent velocity of 30 km s^{-1}, comparable to the velocity dispersion within the disk, this induces to a roughly 10% uncertainty in the inferred $\boldsymbol{\omega}_L$.

The remaining degeneracy with D_L may be broken via the measurement of a parallax from the microlensing event itself. The sources of most interest also are expected to have the longest t_E, and thus encompass a substantial fraction of a year. As made explicit in Figures 6 and 7, long t_E permit measurements of the impact of the Earth's orbital motion, i.e., a parallax. This comes in two forms.

First, the light curve itself is asymmetric as a result of the modified evolution of the Earth-lens-source alignment (Smith et al. 2003). Figure 8 shows the effect of parallax on light curve of a 10 $M_\odot$ black hole lensing event. Since the Earth accelerates substantially during this period, the additional component is distinguishable from the otherwise unknown but essentially fixed velocities of the source and lens, resulting in an asymmetry in the magnification light curve. While the maser emission and optical stellar emission are not spatially coincident, the offset in the distance is much smaller than D_S, and thus D_L can be reconstructed from either the optical or infrared light curves. Typical uncertainties of %10 in radio flux calibration may preclude the use of radio light curve for this purpose. Since Miras are among the brightest stars in the microlensing survey fields, they may be good candidates for obtaining D_L in this way, assuming the underlying variability can be adequately modeled.

Second, as described in the previous section, the underlying impact on the lensed images themselves is directly measurable. Note that this is essentially the same effect, the asymmetry in the magnification light curve arises from the asymmetry in the evolving image structure. However, unlike the parallax effect in the light curve, the image structure is insensitive to the Mira

[7] Recall that a solar-type star would not modify the color of the combined lens-source system sufficiently to place it outside of the allowed region in the CMD.

[8] This may be improved substantially through the exploitation of the impact of parallax on the light curve (Gould 1992; Rahvar et al. 2003).

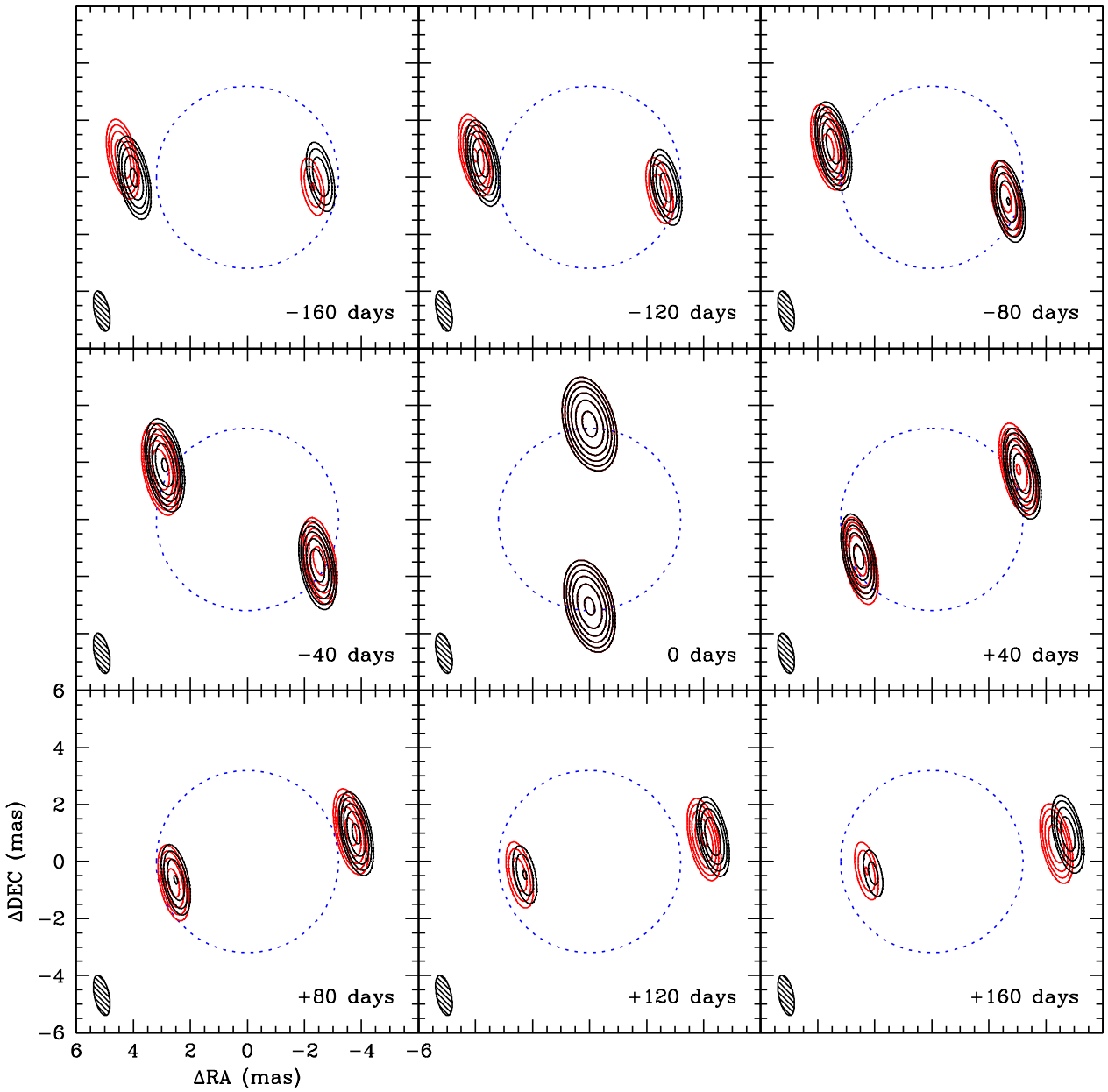

Figure 6. Example 10 $M_\odot$ black hole microlensing event. Impact parameter of 0.3 mas, relative lens-source velocity of 150 km s^{-1}, 1 AU FWHM maser, and radio beam typical of Galactic center observations with the VLBA (semi-minor/major axes of 0.5 mas and 1.4 mas, respectively, with a position angle of 12° east of north). Red contours show images ignoring the orbital motion of the Earth, while black contours include the parallax. For reference, the blue dotted line shows the Einstein ring.

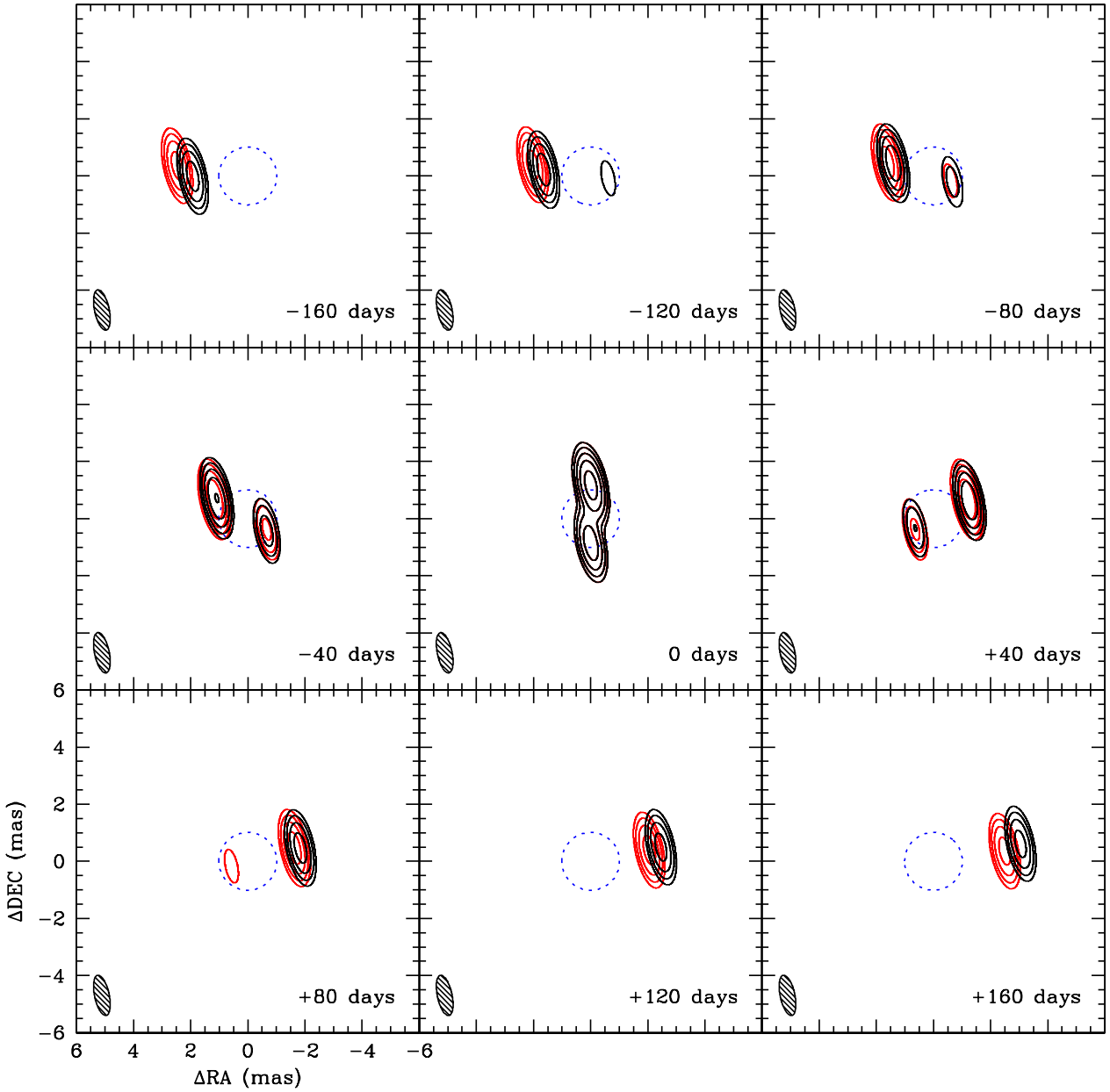

Figure 7. Example 1 $M_\odot$ stellar microlensing event. Impact parameter of 0.3 mas, relative lens-source velocity of 150 km s^{-1}, 1 AU FWHM maser, and radio beam typical of Galactic center observations with the VLBA (semi-minor/major axes of 0.5 mas and 1.4 mas, respectively, with a position angle of 12° east of north). Red contours show images ignoring the orbital motion of the Earth, while black contours include the parallax. For reference, the blue dotted line shows the Einstein ring.

variability. While it is possible to attempt a full fit to the sequence of images, most of the information is contained in the locations of the multiple images. Thus, shown in Figure 9 is the angular separation of image components as a function of time for the sequence of images in Figure 6.

The mock data shown in figure 9 provide a convenient way to estimate the accuracy with which the parallax parameter can be reconstructed. We compute the centroid positions of the multiple image components by performing a maximum-likelihood fit of the positions of beam-convolved point sources. The uncertainty in the centroid is constructed assuming a flux limit of 10% of the maximum brightness of an unlensed maser spot, and introduce corresponding Gaussian fluctuations in the mock data (see in Fig. 9). At late times the uncertainties grow as a result of the dimming of one of the two images far from peak magnification.

As a simple model we write the impact parameter as a linear combination of impact parameters with and without parallax effect included:

$$\beta = \lambda\beta_p + (1-\lambda)\beta_{np}\,, \tag{25}$$

where β_{np} and β_p are the angular separations when the orbital acceleration of the Earth is ignored and included assuming $D_L = D_S/2$. As shown in Appendix A.3, the interpolation parameter is related to the lens distance by $\lambda = (D_S - D_L)/D_L$, and hence a measurement of λ corresponds to a measurement of the lens position. That is, keeping all angular measurements fixed, fitting the evolving image separation directly probes the lens distance.

A maximum-likelihood fit recovers $\lambda = 0.84 \pm 0.20$, where the 1σ errors are indicated. That is, for typical parameters the impact of parallax can be detected within the radio images at more that 4σ. For a given λ the corresponding estimates of the lens distance and its uncertainty are

$$D_L = \frac{D_S}{1+\lambda} \quad \text{and} \quad \frac{\sigma^2_{D_L}}{D_L^2} = \frac{\sigma^2_\lambda}{(1+\lambda)^2}\,, \tag{26}$$

and thus, we recover $D_L = 4.3 \pm 0.5$ kpc. That is, typically, D_L can be reconstructed with an accuracy of roughly 10%.

With an estimate of the lens distance it is possible to reconstruct the lens mass and transverse velocity from θ_E and $\boldsymbol{\omega}_L$. The mass may be estimated given measurements of θ_E and λ via

$$M = \frac{c^2}{4G}\theta_E^2 \frac{D_S}{\lambda}\,. \tag{27}$$

Assuming the uncertainty in θ_E is negligible and in D_S is of order 10%, the fractional uncertainty in M is given by that in λ, and thus the mass can be estimated with an accuracy of roughly 14%. The lens transverse velocity is given by

$$v_L = D_L \boldsymbol{\omega}_L\,. \tag{28}$$

Assuming the typical uncertainties of 10% in both quantities, the transverse velocity can be typically reconstructed to 14% as well.

4.5. *Binaries*

Resolving the lensed images provides a natural way to distinguish between single and double lenses, i.e., isolated and binary black holes. The latter, black hole-black hole binary systems are of particular interest as a potential gravitational wave source (Abadie et al. 2012). At the same time they have the potential to both inform and leverage the observations of X-ray binaries (see, e.g., Remillard & McClintock 2006). Figure 10 shows a typical binary image, which may be immediately distinguished from the Figure 6 by both the complicated lensed-image morphology and, more directly, the presence of a third image.

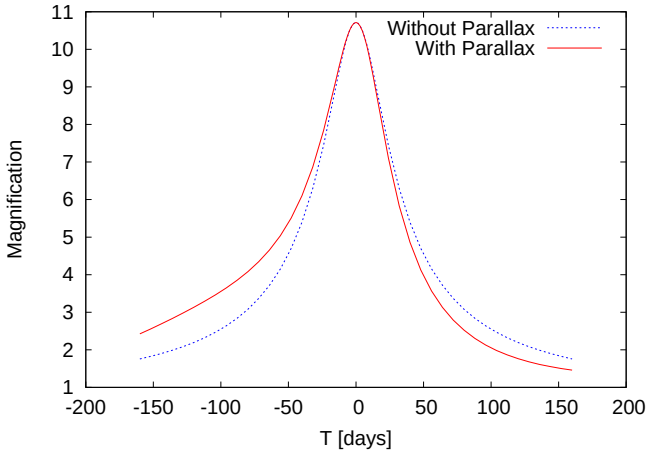

Figure 8. Example light curve for the microlensing event shown in Figure 6. The dashed and solid lines correspond to when the effect of parallax is neglected and included, respectively. On ± 50 day time-scales the impact of parallax is clearly visible, resulting in roughly 30% asymmetries in the light curve.

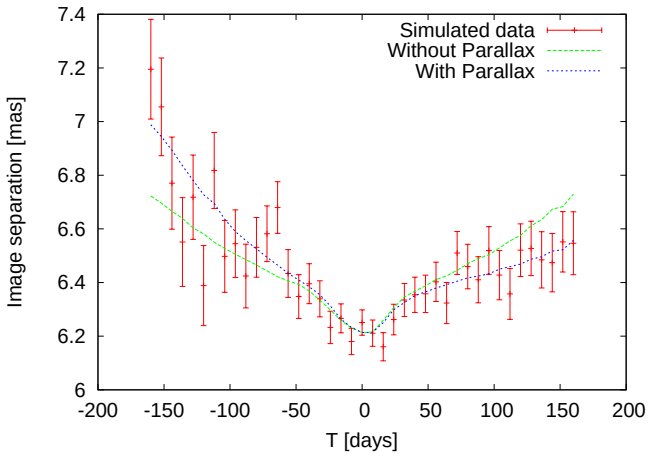

Figure 9. Evolution of the image separations for the microlensing event shown in Figure 6. Centroid errors are constructed assuming a flux limit of 10% the maximum flux. The green long-dashed and blue short-dashed lines correspond to the expected when the image separations when the effect of parallax is neglected and included, respectively. As with the light curve in Figure 8, the largest impact of parallax occurs at early and late times, causing deviations of roughly 50% of a beam width on year time-scales.

The efficiency with which binaries can be detected depends strongly on their projected angular separation. Sufficiently compact binaries will appear as a single lens, while the components of sufficiently wide binaries will produce independent lensing events. After conducting a suite of numerical experiments with binaries in different orientations, peculiar velocities, and impact parameters, we have found that binaries with projected angular separations spanning an order of magnitude about the Einstein angle can be readily identified. The case shown in Figure 10 has a binary angular separation comparable to the individual Einstein radii of the black holes, 3.2 mas.

As with the isolated case, the motion of the Earth induces

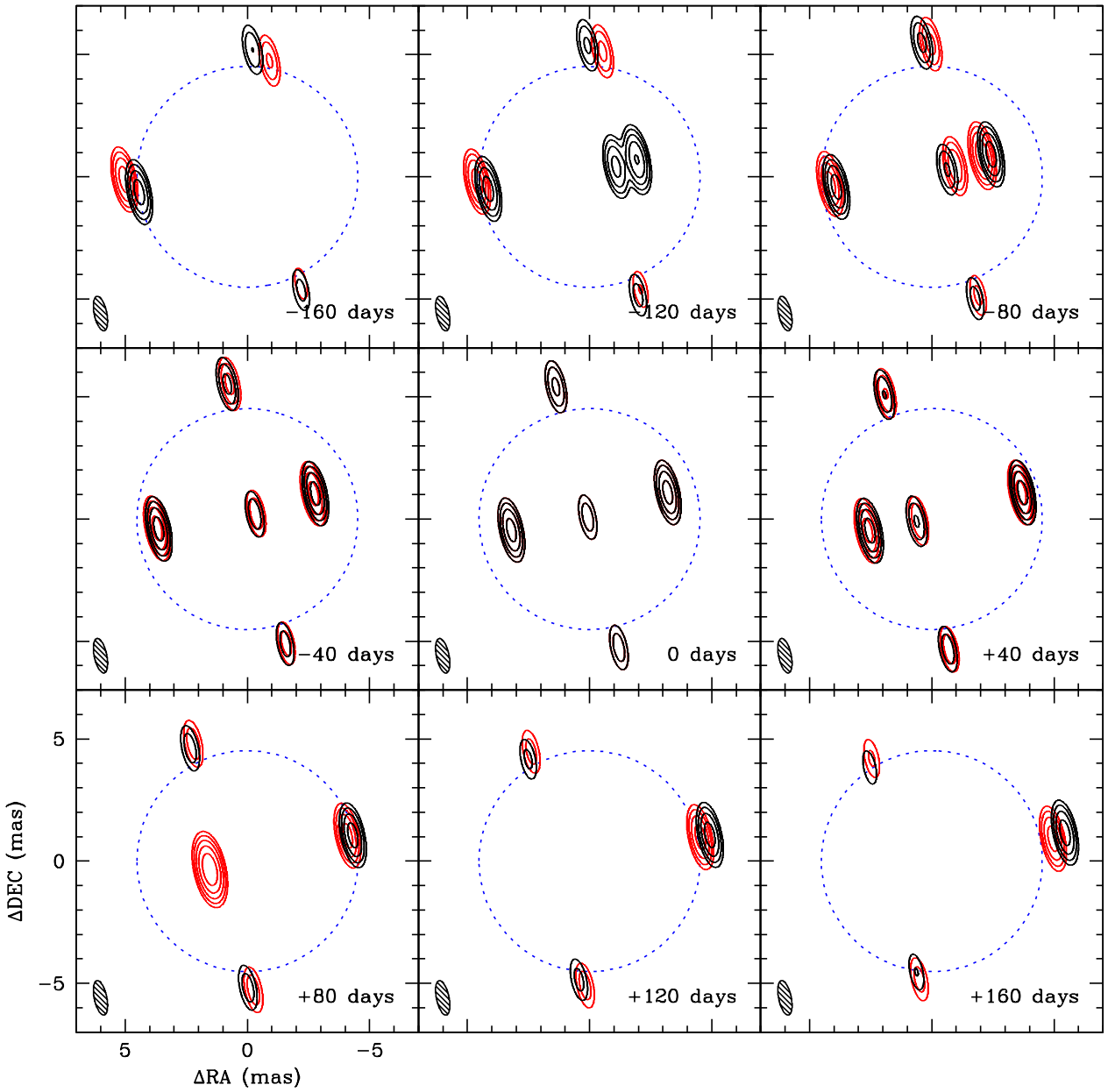

Figure 10. Microlensing event example for a black hole-black hole binary system of equal mass (10 $M_\odot$ each) with orbital period of 30 yr. Impact parameter of 0.3 mas, relative lens-source velocity of 150 km s^{-1}, 1 AU FWHM maser, and radio beam typical of Galactic center observations with the VLBA (semi-minor/major axes of 0.5 mas and 1.4 mas, respectively, with a position angle of 12° east of north). Red contours show images ignoring the orbital motion of the Earth, while black contours include the parallax. For reference, the blue dotted line shows the Einstein ring.

shifts in the image locations due to parallax, and thus the lens distance can in principle be extracted. Unlike the isolated case, typically the image morphology during maximum magnification is complicated. However, as in Figure 9 the parallax signal is dominated shifts at times far from maximum, corresponding to large projected lens-source separations, and thus where the binary will appear most point-like. Nevertheless, we leave binary parameter estimation for future work.

5. DISCUSSION

With moderate changes in strategy existing and future optical/infrared microlensing surveys should achieve black hole event rates of roughly 1.3 yr^{-1}. Dedicated radio microlensing surveys could reach event rates an order of magnitude higher. As a result, radio imaging of microlensing events can provide the novel ability to produce a large sample of stellar remnants with known masses, positions (including distances), and veloc-

ities. Importantly, this sample would not suffer from the standard biases that plague studies based on binaries; the selection effects associated with microlensing surveys are well understood and can be modeled and removed. This enables a variety of probes of astrophysical phenomena, which we discuss here.

5.1. Massive Star Evolution

The large event rates enables the systematic construction of a black hole mass function over a decade. For radio microlensing surveys (see below) this rate can be an order of magnitude larger. Unlike X-ray binaries, for microlensing the observing biases are well understood and can be addressed via direct modeling, resulting in an accurate representation of the mass distribution of stellar mass black holes in the Milky Way.

The mass distribution of black holes would be immediately diagnostic of the dynamics of core collapse supernovae, the cataclysmic events surrounding their formation. Typically, accretion of fallback material produces a mass gap between neutron stars and black holes, a region of relative paucity in the black hole mass function extending to masses well above $2M_{\odot}$ (Timmes et al. 1996; Woosley et al. 2002; Zhang et al. 2008) . In all cases, key uncertainties in the stellar evolution (e.g., wind loss rates, supernovae energetics, etc.) impact the final mass distributions (Gallart et al. 2005). There have been studies on the effect of variations in neutrino mechanism for core collapse supernovae on the theoretical black hole mass function (Pejcha & Thompson 2015) and using the observed black hole mass function there already have been constraints on core collapse supernova (Kochanek 2015). For compact binary systems, the location and depth of the mass gap is further sensitive to the binary evolution history (Fryer et al. 2002). While tentative evidence for a mass gap has already been reported based on the inferred masses of black holes in X-ray binaries (Özel et al. 2010), this is necessarily subject to the variety of strong selection effects and substantial uncertainties mentioned above. Moreover, studies of X-ray binaries are fundamentally limited by the small number of binaries currently known.

In contrast, radio-imaged microlensing events provide a means to systematically accrue large, debiased samples of Galactic black holes, limited only by survey duration. Thus, it offers both a method to assess the poorly known biases inherent in X-ray binaries and ultimately to directly access key elements of massive star evolution.

Furthermore, radio-imaged microlensing events will produce estimates of the lens positions and tangential velocities. Thus, together with the mass function it is possible in principle to construct a Galactic black hole distribution function. The velocity distribution will necessarily be strongly impacted by the dynamics of core collapse supernovae via supernova kicks (Willems et al. 2005), as well as the subsequent evolution of the Galactic remnant population.[9]

Galactic black holes also serve as a fossil record of massive star formation. Therefore, detailed comparisons of the local[10] densities of stellar mass black holes, white dwarfs, and subsolar stars yield an estimate of the potentially temporally and spatially varying stellar initial mass function. In particular, this provides a unique ability to constrain the history of the high-mass end of the initial mass function.

[9] While the dynamical relaxation time of the Galaxy is of order 10^4 Gyr, black holes are much more massive than the typical Galactic object, and thus can have relaxed substantially.

[10] Necessarily accounting for potentially significant differences in relaxation rates.

5.2. Gravitational Wave Experiments

The measurement of the mass of a single isolated stellar-mass black hole would provide an important calibration for population synthesis computations, performed primarily to produce rate estimates for gravitational wave detectors (Belczynski et al. 2002). This is the consequence of the typical nature of lenses in contrast to the particular evolutionary history of X-ray binaries, currently used to calibrate the variety of uncertainties in the rate estimates.

More generally, the binarity rate and source distribution are key inputs into black hole binary gravitational wave source population estimates. High-mass X-ray binaries, the objects likely progenitors of the black hole-black hole binaries visible by experiments like LIGO (Abadie et al. 2010), are necessarily young by virtue of the large mass of the secondary, providing a strong bias towards populations associated with the recent star formation history of the Milky Way. In stark contrast, binary mergers are expected to occur very long times after their formation, and therefore indicative of the integrated star formation history of the Milky Way. The detection of a black hole-black hole binary presents a means to study the binary black hole population over the entirety of the Galactic history. Unfortunately, the lower limit on the projected binary separation for which radio-imaged microlensing events can efficiently detect binarity (roughly 1 mas at 8 kpc) corresponds to orbital periods of years, and thus will not present candidate gravitational wave sources. Nevertheless, it would provide a significant calibration of binary formation rates, and therefore black hole-black hole binary populations.

5.3. Isolated Neutron Stars

Thus far we have focused primarily on black hole lenses. Nevertheless, it is possible to directly detect solar mass objects as well. While we have included a discussion of the white dwarf lensing rates we have largely ignored lensing events from isolated neutron stars. An estimate of the neutron star lensing rate is nevertheless possible using the black hole lensing rate. The two key assumptions are that the massive stellar progenitors of black holes and neutron stars follow a Salpeter initial mass function and that the neutron stars receive kicks during formations.

From the first we estimate the ratio of the total number of Galactic neutron stars to the total number of Galactic black holes:

$$\frac{N_{\rm NS}}{N_{\rm BH}} \approx \left(\frac{M_{\rm ZNS}}{M_{\rm ZBH}}\right)^{-1.35} \approx 4\,, \tag{29}$$

where $M_{\rm ZNS} \approx 8M_{\odot}$ and $M_{\rm ZBH} \approx 21M_{\odot}$ are the minimum zero-age main-sequence masses of stars that form neutron stars and black holes, respectively (Woosley et al. 2002).

The second assumption modifies the volume occupied by neutron stars. Stars formed at an initial radius $r_{\rm init}$ with a natal kick ($v_{\rm kick}$) larger than the circular velocity ($v_{\rm circ}$) will isotropize within a radius of

$$r_{\rm max} \approx r_{\rm init} e^{v_{\rm kick}^2/2v_{\rm circ}^2} \approx 7 r_{\rm init}\,, \tag{30}$$

where we have used typical values $v_{\rm kick} \approx 400$ km s^{-1} and $v_{\rm circ} \approx 200$ km s^{-1}. Thus, neutron stars formed in the Galactic bulge will be distributed across a volume nearly 400 times larger than similarly formed black holes, and thus exhibit a number density 400 times smaller. The net result is that for typical numbers the rate of neutron star microlensing events is

expected to be roughly 1% of that for the black holes, justifying our neglect of neutron stars.

However, we caution that this conclusion is extremely sensitive to the typical kick velocities. If the typical kick velocity is 300 $\mathrm{km\,s^{-1}}$ the neutron star lensing rate rises to 10% of the black hole lensing rate. More importantly, if the neutron star kick velocity distribution contains a low-velocity tail or is bimodal, as suggested by the large number of known Galactic neutron stars (see, e.g., Fryer et al. 1998; Podsiadlowski et al. 2005), the bulge may retain a large fraction of neutron stars originally formed within it. In this cases the neutron star and black hole lensing rates can be comparable. Thus, the relative frequency of neutron star and black hole events provides an additional probe of the distribution of neutron star formation kicks.

If large numbers of neutron star lensing events are observed, radio-imaged microlensing provides a novel way in which to directly measure the neutron star mass function, independent of the biases inherent in the study of neutron star binaries. Unfortunately, given their large typical age ($\gtrsim 1$ Gyr) these are all likely to be exceedingly dim, with luminosities of $\approx 10^{-11}$-$10^{-9} L_{\odot}$, and therefore not amenable to direct size measurements, complicating any effort to directly constrain the high-density nuclear equation of state.

Nominally, these objects would also fall below the death line for typical pulsar magnetic field strengths (10^{12} G) and periods (1 s). However, due to magnetic field decay, implicated by the low surface fields in recycled millisecond pulsars, these objects could still exhibit observable magnetospheric emission; typical surface fields after a Gyr would then be expected to lie near 10^{11} G. Nevertheless, many would still live near the death line, and therefore would at best be transient radio sources. Hence, in this case the radio emission of isolated neutron stars found by radio-imaged microlensing would provide an unbiased probe of neutron star magnetization and its evolution.

6. CONCLUSIONS

VLBI observations of radio-bright microlensing events affords the ability to resolve the multi-component structure of microlensing events at radio wavelengths. Such images would necessarily break the degeneracies between distance, velocity, and source mass inherent in studies of the light curve alone by providing a direct measurement of the size of the Einstein ring and the presence of signatures of parallax in the evolving image structure and/or asymmetric light curves. Thus, radio imaging enables the reconstruction of the lens parameters to better than 15% accuracy. The dominant source of this remaining uncertainty is due to the unknown distance and velocity of the lensed source, and thus these may be improved by roughly an order of magnitude by follow-up observations that constrain the source's proper motion and distance. Furthermore, imaging provides an immediate method to detect binary lenses, albeit within a rather narrow range of orbital separations (corresponding to periods of roughly 2 yr–20 yr. It is noteworthy that this remains the case when the lens belongs to the otherwise unobservable Galactic remnant population, e.g., neutron stars and black holes.

Radio-bright microlensing events can be identified using existing optical/infrared microlensing surveys. Mira variables exhibit SiO masers in their envelops and therefore provide a natural radio-luminous target. Moderate modifications to existing survey strategies, some of which are already pursued by OGLE-IV, should produce events amenable to radio imaging at a rate of $\approx$ 40 $\mathrm{yr^{-1}}$. Of these, assuming the Galactic black hole population arises solely via the evolution of massive stars, roughly 1.3 will due to black holes. This rate will increase substantially if black holes compose a significant fraction of the Galactic dark matter budget.

Detections of Galactic black holes via microlensing provides an unbiased sample of massive star remnants. The existing sample of stellar mass black holes, obtained via observations of X-ray binaries, necessarily suffers from strong, uncertain biases associated with the formation and evolution of tight massive-star binaries. As a consequence, the detection and characterization of even a handful of black holes using radio-imaged microlensing events will inform the late-stage evolution of massive star, the energetics of their subsequent supernovae, and the event rates of current and future gravitational wave experiments.

Currently, the rate of radio-bright microlensing events is limited by the number of compact radio sources above the detection limits of existing VLBI facilities, and in particular the VLBA. Nevertheless, an order of magnitude increase in event rates can be obtained by improvements in the flux limits of VLBI observations, achieved, e.g., through increased collecting area (as could be provided with long baselines in the next-generation VLA), expanded bandwidths and longer integration times, and dedicated radio-continuum microlensing surveys. Therefore, it is possible that in the near future it will be possible to double the number of known Galactic black holes with a survey extending two years, and begin the statistical study of the Galactic black hole properties within a decade.

ACKNOWLEDGEMENTS

The authors would like to thank Andrew Gould, Bryan Gaensler, Geoffry Bower, Simone Portegeis Zwart, Leo Stein, and Niayesh Afshordi for helpful comments and discussions. A.E.B. receives financial support from the Perimeter Institute for Theoretical Physics and the Natural Sciences and Engineering Research Council of Canada through a Discovery Grant. Research at Perimeter Institute is supported by the Government of Canada through Industry Canada and by the Province of Ontario through the Ministry of Research and Innovation.

REFERENCES

Abadie, J., et al. 2010, Classical and Quantum Gravity, 27, 173001
Abadie, J., et al. 2012, Phys. Rev. D, 85, 082002
Alard, C., & Lupton, R. H. 1998, ApJ, 503, 325
Alcock, C., et al. 1995, ApJL, 454, L125
—. 2001, ApJL, 550, L169
Backer, D. C. 1978, ApJL, 222, L9
Bandura, K., et al. 2014, in Society of Photo-Optical Instrumentation Engineers (SPIE) Conference Series, Vol. 9145, Society of Photo-Optical Instrumentation Engineers (SPIE) Conference Series, 22
Bartelmann, M. 2010, Classical and Quantum Gravity, 27, 233001
Belczynski, K., Kalogera, V., & Bulik, T. 2002, ApJ, 572, 407
Binney, J., & Tremaine, S. 1987, Galactic dynamics
Bower, G. C., Goss, W. M., Falcke, H., Backer, D. C., & Lithwick, Y. 2006, ApJL, 648, L127
Chabrier, G. 2003, PASP, 115, 763
Condon, J. J. 1984, ApJ, 287, 461
Condon, J. J., Cotton, W. D., Greisen, E. W., et al. 1998, AJ, 115, 1693
Condon, J. J., et al. 2012, ApJ, 758, 23
Fryer, C., Burrows, A., & Benz, W. 1998, ApJ, 496, 333
Fryer, C. L., Belczynski, K., Wiktorowicz, G., et al. 2012, ApJ, 749, 91
Fryer, C. L., Heger, A., Langer, N., & Wellstein, S. 2002, ApJ, 578, 335
Gallart, C., Zoccali, M., & Aparicio, A. 2005, Annu. Rev. Astron. Astrophys., 43, 387
Gaudi, B. S. 2012, ARA&A, 50, 411
Gould, A. 1992, ApJ, 392, 442
—. 2000, ApJ, 535, 928
—. 2014, Journal of Korean Astronomical Society, 47, 215

Gwinn, C. R., Kovalev, Y. Y., Johnson, M. D., & Soglasnov, V. A. 2014, ApJL, 794, L14
Hartwick, F. D. A. 2004, ApJ, 603, 108
Henderson, C. B., Gaudi, B. S., Han, C., et al. 2014, ApJ, 794, 52
Heyl, J. S. 2011, MRAS, 411, 1780
Hobbs, G., Lorimer, D. R., Lyne, A. G., & Kramer, M. 2005, MNRAS, 360, 974
Ivezic, Z., et al. 2008, arXiv:0805.2366, arXiv:0805.2366
Kholopov, P. N. 1990, General catalogue of variable stars. Vol.4: Reference tables
Kochanek, C. S. 2015, MNRAS, 446, 1213
Kroupa, P. 2001, MNRAS, 322, 231
Lasserre, T., et al. 2000, A&A, 355, L39
Lu, R.-S., Krichbaum, T. P., Eckart, A., et al. 2011, A&A, 525, A76
Matsunaga, N., Fukushi, H., & Nakada, Y. 2005, MNRAS, 364, 117
Miyake, N., et al. 2011, ApJ, 728, 120
Moniez, M. 2010, General Relativity and Gravitation, 42, 2047
Muraki, Y., et al. 2011, ApJ, 741, 22
Özel, F., Psaltis, D., Narayan, R., & McClintock, J. E. 2010, ApJ, 725, 1918
Paczynski, B. 1986, ApJ, 304, 1
Pejcha, O., & Thompson, T. A. 2015, ApJ, 801, 90
Pen, U.-L., Macquart, J.-P., Deller, A. T., & Brisken, W. 2014, MNRAS, 440, L36
Persic, M., Salucci, P., & Stel, F. 1996, MNRAS, 281, 27
Podsiadlowski, P., Pfahl, E., & Rappaport, S. 2005, in Astronomical Society of the Pacific Conference Series, Vol. 328, Binary Radio Pulsars, ed. F. A. Rasio & I. H. Stairs, 327
Poteet, W. M., Cauthen, H. K., Kappler, N., et al. 2012, in Society of Photo-Optical Instrumentation Engineers (SPIE) Conference Series, Vol. 8444, Society of Photo-Optical Instrumentation Engineers (SPIE) Conference Series
Rahvar, S. 2015, International Journal of Modern Physics D, 24, 30020
Rahvar, S., Moniez, M., Ansari, R., & Perdereau, O. 2003, A&A, 412, 81
Refregier, A. 2003, ARA&A, 41, 645
Reid, M. J., & Goldston, J. E. 2002, ApJ, 568, 931
Reid, M. J., Menten, K. M., Genzel, R., et al. 2003, ApJ, 587, 208
Reid, M. J., Menten, K. M., Trippe, S., Ott, T., & Genzel, R. 2007, ApJ, 659, 378
Remillard, R. A., & McClintock, J. E. 2006, Annual Review of Astronomy and Astrophysics, 44, 49
Robin, A. C., Reylé, C., Derrière, S., & Picaud, S. 2003, A&A, 409, 523
Salaris, M., Serenelli, A., Weiss, A., & Miller Bertolami, M. 2009, ApJ, 692, 1013
Schultheis, M., Ramírez, S., Sellgren, K., Stolovy, S., & Ganesh, S. 2009, in The Evolving ISM in the Milky Way and Nearby Galaxies, 59
Shan, H. Y., et al. 2014, MNRAS, 442, 2534
Smith, B. J., Leisawitz, D., Castelaz, M. W., & Luttermoser, D. 2002, AJ, 123, 948
Smith, M. C., Mao, S., & Paczyński, B. 2003, MNRAS, 339, 925
Soszyński, I., et al. 2013, AcA, 63, 21
Street, R. A., et al. 2015, ArXiv e-prints, arXiv:1508.07027
Sumi, T., et al. 2003, ApJ, 591, 204
Taylor, A. 2007, Proceedings of the International Astronomical Union, 3, 164
Timmes, F. X., Woosley, S. E., & Weaver, T. A. 1996, ApJ, 457, 834
Udalski, A., Szymanski, M., Kaluzny, J., et al. 1994, AcA, 44, 227
Udalski, A., Szymański, M. K., & Szymański, G. 2015, AcA, 65, 1
Whitney, A. R., et al. 2012, ArXiv e-prints, arXiv:1210.5961
Willems, B., Henninger, M., Levin, T., et al. 2005, ApJ, 625, 324
Witt, H. J., & Mao, S. 1994, ApJ, 430, 505
Wood, P. 2006, Proceedings of the International Astronomical Union, 2, 343
Woosley, S. E., Heger, A., & Weaver, T. A. 2002, Reviews of Modern Physics, 74, 1015
Wyrzykowski, Ł., et al. 2015, ApJS, 216, 12
Zhang, W., Woosley, S. E., & Heger, A. 2008, ApJ, 679, 639

APPENDIX

A. BREAKING DEGENERACY WITH COMBINED OBSERVATION

In this section we introduce the mathematical basis of gravitational microlensing, introduce the photometric and astrometric observations of microlensing events and the way we can break the degeneracy between the lens parameters.

A.1. Lens Equation for Single Lens

Single lens equation is given by geometrical relation between the angular position of source β, angular position of the image θ and Einstein angle θ_E as follows:

$$\theta^2 - \theta\beta - \theta_E^2 = 0, \tag{A1}$$

where β and θ are given with respect the center of coordinate system where lens is located. In the gravitational microlensing β changes with time on a straight line as

$$\beta^2 = \beta_0^2 + \theta_E^2 (\frac{t-t_0}{t_E})^2, \tag{A2}$$

where β_0 is the minimum impact factor and t_0 is the time of closest angular approach of the lens and source. From the equation (A1), we get two solutions for the position of two images at two sides of the lens as follows:

$$\theta^{\pm} = \frac{\beta \pm \sqrt{\beta^2 + 4\theta_E^2}}{2}. \tag{A3}$$

Substituting equation (A2) in equation(A3) results in the radial dynamics of the images as a function of time.

The angular distance between the two images ($\Delta\theta = \theta^+ - \theta^-$), regardless of the position of source, can be written in terms of the impact parameter and the Einstein angle:

$$\Delta\theta = \sqrt{\beta^2 + 4\theta_E^2} \tag{A4}$$

At the minimum impact parameter where $\beta = \beta_0$, two images get nearest approach to each other and in this case the trajectory of the source is perpendicular to the line connecting these two images

$$\beta_0 = \sqrt{\Delta\theta^2 - 4\theta_E^2}. \tag{A5}$$

We note that on the right hand side the term in the square-root should be positive which implies $\Delta\theta \geq 2\theta_E$. So the separation between the two images is always larger than the diameter of Einstein ring while one image is inside and the other one is outside the Einstein ring.

The other observable parameter which can be measured from the photometry is the magnification of the source during the lensing. Since in the gravitational lensing the flux of light is conserved, the apparent change of area for lensed images would lead to a change in the energy we receive from each image. The area of images compared to the source size is given by the inverse of determinant of Jacobian. Denoting the area for the two images by A^+ and A^- the differential element of area of an image to that of the source is given by:

$$A^{\pm} = \frac{\theta^{\pm}}{\beta}\frac{\partial\theta^{\pm}}{\partial\beta}. \tag{A6}$$

Substituting equation (A3) in equation(A6) the area for each images could be written as:

$$A^{\pm} = \frac{1}{2}(\frac{\beta^2 + 2\theta_E^2}{\beta\sqrt{\beta^2 + 4\theta_E^2}} \pm 1) \tag{A7}$$

The overall magnification is the sum of these two terms,

$$A = |A^+| + |A^-| = \frac{\beta^2 + 2\theta_E}{\beta\sqrt{\beta^2 + 4\theta_E^2}}. \tag{A8}$$

Substituting equation for (A2) the magnification is independent of Einstein angle and only depends on t_0, t_E and $u_0 = \beta_0/\theta_E$.

At the time of minimum approach the magnification would have its maximum as a function of β_0 and θ_E. Substituting β_0 from equation (A5) in (A8), maximum magnification can be obtained as a function of Einstein angle and angular separation

between the images as follows:

$$A_{\max} = \frac{\Delta\theta^2 - 2\theta_E^2}{\Delta\theta\sqrt{\Delta\theta^2 - 4\theta_E^2}} \tag{A9}$$

As a result the Einstein angle can be directly extracted from $A_{\max}$ as described in equation (22).

If the distance of the source from earth is known (which is the case for microlensing events in Galactic center) measuring θ_E can put constrains on the mass and the lens distance from observer. On the other hand parallax measurements can impose another constrain on the lens parameters and in theory can resolve the lens parameters.

A.2. Parallax Effect in Microlensing Light Curves

The microlensing parallax effect results from the accelerating motion of the earth around sun. It manifests itself as the relative motion of the source with respect to lens deviates from a straight line. Assuming earth moves around the sun in a circular orbit, the relative angular motion of the lens and source with respect to the observer in the case of stationary source and lens is given by

$$\pi_x = \pi\cos\xi(t), \tag{A10}$$
$$\pi_y = \pi\cos\beta\sin\xi(t), \tag{A11}$$

where

$$\pi = \frac{1}{\theta_E}\left(\frac{1a.u.}{D_l} - \frac{1a.u.}{D_s}\right), \tag{A12}$$

β is the angular deviation of the orbital plane with respect to our line of sight, $\xi(t) = \omega t + \xi_0$, ω is the orbital angular frequency and ξ_0 is the initial phase of the earth orbit which can be set to zero at the equinox. On the other hand relative displacement of the source with respect to position of the sun on the lens plane is given by

$$\beta_x^S = \beta(t)\cos\alpha - \beta_0(\cos\alpha + \sin\alpha), \tag{A13}$$
$$\beta_y^S = \beta(t)\sin\alpha + \beta_0(\cos\alpha - \sin\alpha), \tag{A14}$$

where the superscript represents relative motion of the source with respect to the sun and β_0 is the closest approach of the source to the sun and α is the angle between the trajectory of source and semi-major axis of the earth orbit. Now combining these two motions the relative motions of the source with respect to the earth is given by

$$\vec{\beta}(t) = \vec{\beta^S}(t) - \vec{\pi}(t). \tag{A15}$$

The second term corresponds to a perturbation compared to the simple microlensing events. The photometric effect of parallax can be measured as an asymmetry of the microlensing light curve (Alcock et al. 1995). Also the astrometric effect of parallax is observable, if the lensed images are resolved. By combining equation (22) and (A12) the distance of lens from the observer (D_l) can be extracted. Substituting in the definition of θ_E, the mass of lens can be obtained. In fact the lens mass can be obtained only given θ_E and π_r using the relation:

$$\frac{M}{M_\odot} = \frac{1}{8\pi_r}\left(\frac{\theta_E}{1\ \text{mas}}\right). \tag{A16}$$

From photometric observations and microlensing light curves the physical parameter that is obtained by fitting to the light curve is the Einstein crossing time. Having measured this parameter the transverse velocity of lens can be derived as $v_t = D_l\theta_E/t_E$.

A.3. Parallax Effect in Microlensing Images

The acceleration of the Earth impacts the image separations for the same reason it affects the light curve. Here we estimate the size of this effect, explicitly determining the way in which the lens distance enters.

We begin by defining averaged and perturbed lens and source positions,

$$s \equiv x_S - x_\oplus = \bar{s} - \boldsymbol{\delta} \quad \text{and} \quad \boldsymbol{\ell} \equiv x_L - x_\oplus = \bar{\boldsymbol{\ell}} - \boldsymbol{\delta}, \tag{A17}$$

where $\bar{s}$ and $\bar{\boldsymbol{\ell}}$ include the linear lens and source motions and the linear component of the Earth's motion. The acceleration of the Earth is contained in $\boldsymbol{\delta}$ which is by construction quadratic in time to lowest order. We will presume this to be small in comparison to $\bar{s}$ and $\bar{\boldsymbol{\ell}}$.

Inserting these into equation (16) and linearizing in $\boldsymbol{\delta}$ and ignoring terms of order β^2 yields

$$\begin{aligned}\boldsymbol{\beta} &\equiv \left(\mathbf{1} - \frac{\boldsymbol{\ell}\boldsymbol{\ell}}{D_L^2}\right)\cdot\frac{s}{D_S} \\ &\approx \left(\mathbf{1} - \frac{\bar{\boldsymbol{\ell}}\bar{\boldsymbol{\ell}}}{D_L^2}\right)\cdot\frac{\bar{s}}{D_S} \\ &\quad + \left(\frac{D_S}{D_L} - 1\right)\left(\mathbf{1} - \frac{\bar{\boldsymbol{\ell}}\bar{\boldsymbol{\ell}}}{D_L^2}\right)\cdot\frac{\boldsymbol{\delta}}{D_S} \\ &\quad + \frac{\bar{\boldsymbol{\ell}}}{D_L}\frac{\bar{s}}{D_L}\cdot\left(\mathbf{1} - \frac{\bar{\boldsymbol{\ell}}\bar{\boldsymbol{\ell}}}{D_L^2}\right)\cdot\frac{\boldsymbol{\delta}}{D_S}.\end{aligned} \tag{A18}$$

Therefore, noting that $\boldsymbol{\beta}\cdot\boldsymbol{\ell} = 0$,

$$\beta \approx \beta_{np} + \left(\frac{D_S - D_L}{D_L}\right)\frac{\boldsymbol{\beta}_{np}}{\beta_{np}}\cdot\frac{\boldsymbol{\delta}}{D_S}, \tag{A19}$$

where $\boldsymbol{\beta}_{np} \equiv \left(\mathbf{1} - \bar{\boldsymbol{\ell}}\bar{\boldsymbol{\ell}}/D_L^2\right)\cdot\bar{s}/D_S$ is the angular position of the lens ignoring the Earth's acceleration. The corresponding angular separation between the multiple images is then given by equation (A4)

$$\Delta\theta \approx \Delta\theta_{np} + \left(\frac{D_S - D_L}{D_L}\right)\frac{\boldsymbol{\beta}_{np}}{\Delta\theta_{np}}\cdot\frac{\boldsymbol{\delta}}{D_S}. \tag{A20}$$

Note that equation (A19) interpolates between β_{np} and β as the lens distance changes. With the definition

$$\beta_p \equiv \beta_{np} + \frac{\boldsymbol{\beta}_{np}}{\beta_{np}}\cdot\frac{\boldsymbol{\delta}}{D_S}, \tag{A21}$$

i.e., when $D_L = D_S/2$, we recover equation (25),

$$\beta = \lambda\beta_p + (1-\lambda)\beta_{np}, \tag{25}$$

where

$$\lambda \equiv \frac{D_S - D_L}{D_L}. \tag{A22}$$